Rytömaa, Samuli; Malmi, Olli; Laine, Sampo; Keinänen, Jarkko; Viitala, Raine

Wire rope isolator identification and dynamic modeling for small amplitude vibrations

Published in:
Engineering Structures

DOI:
10.1016/j.engstruct.2024.118721

Published: 01/11/2024

Document Version
Publisher's PDF, also known as Version of record

Engineering Structures 318 (2024) 118721

Contents lists available at ScienceDirect

Engineering Structures

journal homepage: www.elsevier.com/locate/engstruct

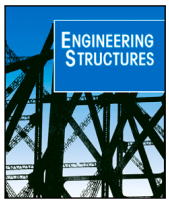

Wire rope isolator identification and dynamic modeling for small amplitude vibrations☆

Samuli Rytömaa [a,*], Olli Malmi [b], Sampo Laine [a], Jarkko Keinänen [b], Raine Viitala [a]

[a] Department of Mechanical Engineering, Aalto University, Espoo, Finland
[b] Vibrol Oy, Tuusula, Finland

ARTICLE INFO

Keywords:
Structural dynamics
Damping model
Vibration
Wire rope isolator
Rate-independent model

ABSTRACT

Wire rope isolators are used in variety of applications to protect sensitive equipment from vibration. The nonlinear hysteretic behavior of steel wires provides advantages when compared to linear vibration isolators. This study proposes an amplitude dependent stiffness and damping model for low amplitude vibrations under axial loading, where the parameters can be determined with an experimental procedure. Comprehensive experimental results of forced vibration tests with varying loading, frequency and preload were considered in the model identification. Amplitude dependent stiffness and loss energy models were determined from the test data, and the effect of the preload and loading frequency on the model parameters were studied. It is shown, that the effect of preload and frequency is not evidently clear, while the effect of vibration amplitude is more significant. The mathematical model was further verified against measurements from base excitation loading. The proposed model can be used to study the effectiveness of the selected wire rope isolator configurations in chosen application, and to effectively perform dynamic design studies.

1. Introduction

Passive vibration isolators are used to protect sensitive equipment from vibrations sources, such as the excitation from heavy machinery, or from seismic loads. Previous research has shown that passive isolators with nonlinear properties, the frequency band of the vibration isolation is typically larger in comparison to linear isolators [1–5]. The wire rope isolator (WRI) is a type of passive isolator, made by joining two metal pieces together using steel wire as seen in Fig. 1, which acts as a nonlinear spring with internal damping. The number and size of wire rope loops and wire rope dimensions can vary greatly, and they all affect the dynamics of the WRI. In addition to the wire rope parameters, the wire rope formation such as the height, width and number of loops and their vertical angle can be varied in application specific designs, to sustain loads in chosen directions and frequency ranges.

The mechanical behavior of WRI is characterized by the hysteresis, which arises from the internal friction inside and between the wire strands [6]. With small deformations, the wires of the strand stick to each other, but eventually start to slip, which dissipates energy [7]. When the amplitude of deformation increases, the wires at the edge of the strands begin to slip first [8]. With larger amplitude, more wires start to slip, causing the characteristic nonlinear damping properties of the WRI. The slip of wires and strands decreases the bending stiffness of the wire rope element [9,10]. These two mechanisms contribute to the nonlinear response of the WRI.

The WRI deforms differently with different loading directions, as the loading direction affects the method at which the wire rope loops resist the deformation [11]. The principal loading directions are shown in Fig. 2. In the horizontal loading (roll and shear) the hysteresis loop is symmetric, but in vertical loading (axial loading, y-axis in Fig. 1) the hysteresis loop is asymmetric between tension and compression [12,13]. In the case of vertical loading, the stiffness is higher on the tensile side of the hysteresis loop. The amount of asymmetry of the hysteresis loop grows with increasing amplitude [13]. The behavior of WRIs under roll and shear directions has also been studied [13,14].

Several mathematical models have been developed to characterize the behavior of WRIs. The focus of recent research has been on modeling the dynamics using models derived from the Bouc–Wen hysteresis model [15,16], which account for the asymmetric hysteresis loop shapes of the WRI in axial direction [13,17,18]. Another method is utilization of experimentally measured frequency response curves [19]. Several studies have investigated the performance of WRI as a seismic isolator [14,19–25]. In seismic isolation, the focus is on response with low frequencies and high amplitudes. In case of vibration attenuation of machinery, the focus is primarily on lower vibration amplitudes and

☆ Funding: The research was funded by Business Finland (Power Beyond, grant number 2534/31/2022).
* Corresponding author.
E-mail address: samuli.rytomaa@aalto.fi (S. Rytömaa).

https://doi.org/10.1016/j.engstruct.2024.118721
Received 10 April 2024; Received in revised form 24 June 2024; Accepted 30 July 2024
Available online 7 August 2024

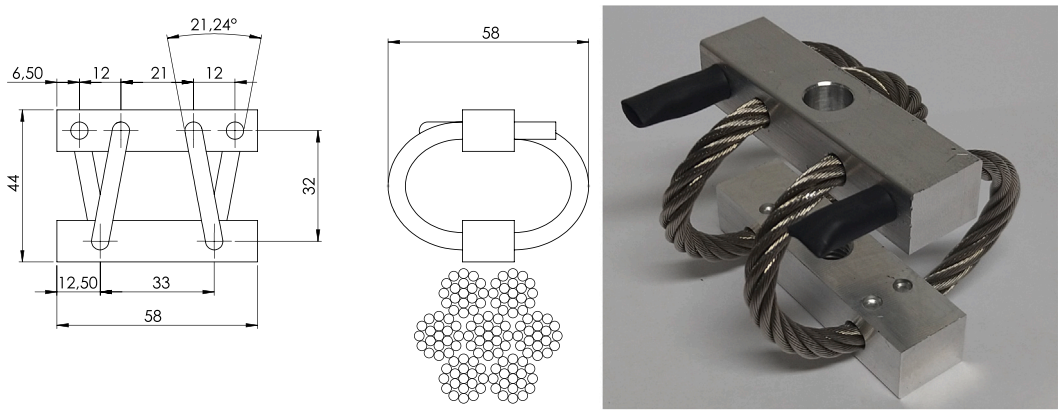

Fig. 1. The considered wire rope isolator and schematic of its main dimensions. The wire rope diameter is 5 mm. Cross-section of the wire ropes consists of seven strands, with nineteen wires each.

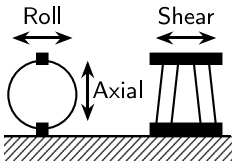

Fig. 2. Naming of the different WRI loading directions. This study focuses on the axial direction.

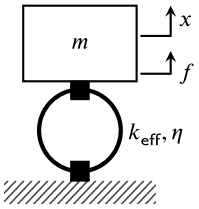

Fig. 3. Mathematical model for a single degree of freedom model of the WRI.

higher frequencies, thus the requirements for dynamic modeling are slightly different. These have been investigated in [6,17,26]. The use of WRIs to dampen wind-induced vibrations in bridge stay cables has been performed by [27]. Previous research on wire rope isolators and mechanics has been summarized by [28] and by [29].

While accurate models have been developed to model the dynamics of WRI, they are highly complex due to the fundamental nonlinearities arising from the deformation and energy dissipation mechanisms. For practical design work, less complex models which provide adequate results are needed. These models should be simple to use and the parameters easily identified, as the number of different WRI configurations is large. Commonly, isolated equipment is placed on top of the WRIs, and thus the effect of the supported load on the dynamics must be considered. To efficiently select the best WRI for each application, a large number of dimensions and configurations need to be evaluated. With simpler models, this can be done efficiently, allowing faster delivery times.

This study proposes a new model for the steady-state axial response of wire rope isolators under small amplitude vibrations. The model considers the nonlinear response of the WRI using amplitude based linearization. Industry standard testing setup was used to determine the model parameters. The model improves the current body of knowledge by providing a better fit under small amplitudes of vibration compared to models with similar complexity. In addition to the mathematical model, comprehensive experimental results were carried out with three different levels of preload and six loading frequencies. The proposed model is shown to have good agreement with measured response under base excitation.

2. Proposed mathematical model for wire rope isolators

In this study the WRI is modeled as a single degree-of-freedom nonlinear element. The damping and stiffness of the proposed model depend on the vibration amplitude. This means that the element stiffness is linearized with respect to the vibration amplitude. Illustration of the system is presented in Fig. 3. For linear elements, energy loss is commonly included as viscous damping, but complex stiffness is an effective alternative for damping mechanisms, which do not depend on the rate of deformation [30]. It should be noted, that the complex stiffness method is only applicable for steady-state problems. The equations of motion for a single-DOF model with viscous damping (1) and complex stiffness (2) are

$$m\ddot{x} + c\dot{x} + kx = f \quad \text{viscous damping} \tag{1}$$

$$m\ddot{x} + (1 + i\eta)kx = f \quad \text{complex stiffness} \tag{2}$$

where m is the mass supported by the spring, k is the stiffness, c is the viscous damping coefficient, i is the imaginary unit, η is the loss factor, x is the displacement and f is the external force. In these equations, k, c and η depend on the vibration amplitude. Because WRI has mostly amplitude dependent nonlinearity [6], the proposed model is based on the complex stiffness approach, which better reflects the nonlinear energy loss mechanism of the WRI. In steady-state analyses, the differences between the two methods are small. The following subsections present the nonlinear formulation for the loss factor and stiffness.

2.1. Damping

There are two major energy dissipation mechanisms involved with the wire rope isolators, as proposed by [26]. Coulomb friction due to the rubbing of the wires and strands, and the material damping due to the material bending. The hypothesis of this study is that the frictious losses are prevalent at higher amplitudes, where more relative motion occurs, and the material damping is prevalent in lower vibration amplitudes with less relative motion of the strands. The relative motion between strands also decreases the total stiffness of the WRI, as sliding contact provides less resistance than sticking.

Damping of the WRI is assumed to originate from two sources, coulomb friction and material damping. Energy loss from coulomb friction during single cycle is linearly proportional to the vibration amplitude, while the energy loss due to material damping is proportional

to the square of the vibration amplitude. Other way on perceiving the material damping is the linear increase of sliding surface area inside the wire ropes as a function of amplitude. In [26], the same two phenomena were considered for energy loss, but they were acting simultaneously. In this study, material damping is assumed to be initially dominant at lower vibration amplitude, but its effect diminishes at higher amplitudes, when the friction losses become dominant. This can also be viewed that at some point the increase of friction area saturates, leading to solely linearly proportional damping. To model this phenomenon, the energy loss needs to be defined differently for the two regions.

In the proposed modeling approach, a piecewise function is fitted to measured loss energy of the WRI as a function of vibration amplitude. Here, the loss energy is defined as the amount of energy dissipated during a single cycle of steady-state vibration. Initially, the loss energy follows a second order polynomial as a function of amplitude. The second order term represents the material damping, while the first order term models friction losses. The constant term represents the initial slipping distance, before which the WRI behaves linearly, i.e., the amplitude when the wires begin to slip. This linearity is ensured by defining that the W_{loss} value cannot be negative. Otherwise damping term would increase the system energy, which is obviously impossible. After a certain amplitude threshold, the loss energy starts to increase linearly. Coulomb damping is the dominant phenomena in this region. The loss energy model for one oscillation cycle is defined as

$$W_{loss}(x_a) = \begin{cases} a_1 x_a^2 + b_1 x_a + c_1, & x_a < x_{\text{threshold}} \\ b_2 x_a + c_2, & x_a \geq x_{\text{threshold}}, \end{cases} \qquad W_{\text{loss}} \geq 0 \tag{3}$$

where x_a is the vibration amplitude of the WRI or the relative movement between the WRI ends. The values for the coefficients a_1, b_1, c_1, b_2, c_2, and $x_{\text{threshold}}$ are determined with a curve fitting procedure from the measured loss energy. Namely, the amount of energy dissipated at a given vibration amplitude, which is calculated from the area of measured hysteresis loops. Because the amplitude dependent loss energy terms are physical quantities, their values must be positive to ensure sensible energy dissipation properties. The constant term c_2 of the linear function is selected so that the function is continuous at the change of regime. The function is not necessarily differentiable at this point.

2.2. Stiffness

The effective stiffness k_{eff} of the WRI changes as a function of vibration amplitude. Here, the effective stiffness is considered, which is defined from the extreme values of the measured hysteresis loop. When dynamic loading in axial direction is considered, the response is different on the tension and compression sides of the hysteresis loops. Neutral state between compression and tension states is at static equilibrium. On the compression side of the hysteresis curve the stiffness decreases, while on the tension side the effective stiffness initially decreases [26]. At certain vibration amplitude, the effective stiffness starts to increase again [26]. The proposed model assumes a symmetric hysteresis curve. This is assumption justified by the fact that the model is created for small amplitudes, where the hysteresis curve has almost identical on both tension and compression sides.

In the presented model, a third order polynomial is fitted based on the measured effective stiffness.

$$k_{\text{eff}}(x_a) = a x_a^3 + b x_a^2 + c x_a + d \tag{4}$$

where a, b, c and d are parameters that are fitted to measured data. In [26], the effective stiffness was determined using representative amplitude from the measurements, which is also the method used in the present study. Representative amplitude is

$$x_a = \sqrt{x_{a\text{C}} x_{a\text{T}}} \tag{5}$$

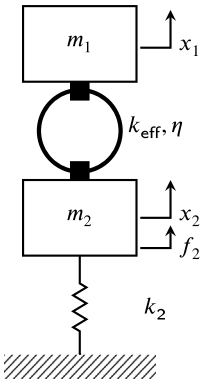

Fig. 4. Mathematical model for a two degree of freedom base excitation setup.

where $x_{a\text{C}}$ is the amplitude on the compression side and $x_{a\text{T}}$ is the amplitude on the tension side of the hysteresis curve. The same equation is used to calculate the representative force. The representative amplitude and force are then used to calculate the effective stiffness at each vibration amplitude.

To use the complex stiffness, the loss factor η needs to be calculated. This is the ratio between dissipated energy W_{loss} during one vibration cycle and elastic energy $W_{elastic}$ at maximum amplitude:

$$\eta = \frac{W_{\text{loss}}(x_a)}{W_{\text{elastic}}(x_a)} \tag{6}$$

For hysteretic systems, elastic energy is calculated from the vibration amplitude and the corresponding effective stiffness

$$W_{\text{elastic}}(x_a) = \frac{1}{2} k_{\text{eff}}(x_a) x_a^2 \tag{7}$$

where k_{eff} is the effective stiffness and x_a is the vibration amplitude.

2.3. System model

The proposed WRI model can be easily included in the standard dynamic equation of motion using complex stiffness. For a single-DOF model where a mass is supported on top of WRI (c.f. Fig. 3), the equation of motion is

$$m\ddot{x} + k_{\text{eff}}(x_a)(1 + i\eta(x_a))x = f, \quad x = x_a e^{i\omega t + i\theta}, \quad f = f_0 e^{i\omega t} \tag{8}$$

where f is the excitation force and m is the mass supported by the WRI. The stiffness k_{eff} and loss factor η are functions of WRI amplitude x_a. For more complex systems with two or more degrees of freedom, the equations of motion are

$$\mathbf{M}\ddot{\mathbf{x}} + (\mathbf{K}(x_a) + \mathbf{K}_{\text{WRI}}(x_a) i\eta(x_a))\mathbf{x} = \mathbf{f} \tag{9}$$

where $\mathbf{M}$ and $\mathbf{K}$ are the system mass and stiffness matrices, $\mathbf{K}_{\text{WRI}}$ is part of the system stiffness matrix related to WRI, η is the loss factor, $\mathbf{f}$ is the force vector. In the case of a two degree of freedom model for base excitation study, (c. f. Fig. 4) the equations of motion are

$$\begin{bmatrix} m1 & 0 \\ 0 & m2 \end{bmatrix} \ddot{\mathbf{x}} + \begin{bmatrix} k_{\text{eff}}(x_a)(1 + i\eta(x_a)) & -k_{\text{eff}}(x_a)(1 + i\eta(x_a)) \\ -k_{\text{eff}}(x_a)(1 + i\eta(x_a)) & k_{\text{eff}}(x_a)(1 + i\eta(x_a)) + k_2 \end{bmatrix} \mathbf{x} = \begin{bmatrix} 0 \\ F_2 \end{bmatrix} \tag{10}$$

$$\mathbf{x} = \begin{bmatrix} x_1 e^{i\phi_1} \\ x_2 e^{i\phi_2} \end{bmatrix} e^{i\omega t} \tag{11}$$

where m_2 is the base mass and k_2 is the stiffness of the springs supporting the base. This type of system is used to verify the model by comparison to experimental results.

Table 1
General parameters used in the validation of the mathematical model. Values have been selected arbitrarily, and are not based on anything physical.

Parameter	Value
m	0.1 kg
F_{max}	2000 N
$x_{threshold}$	1.5 m

Table 2
Coefficients for the loss energy function used in the validation of the mathematical model. Values have been selected arbitrarily, and are not based on anything physical.

Parameter	Value
a_1	200 J/m^3
b_1	1 J/m^2
c_1	−12.5 J/m
b_2	440 J/m^2
c_2	2.221 J/m

Table 3
Coefficients for the effective stiffness polynomial used in the validation of the mathematical model. Values have been selected arbitrarily, and are not based on anything physical.

Parameter	Value
a	4.8 N/m^4
b	64.5 N/m^3
c	−293.3 N/m^2
d	550.9 N/m

The WRI vibration amplitude can be calculated using the following equation, which takes into account the phase difference between the two masses.

$$x_a = |x_1 e^{i\phi_1} - x_2 e^{i\phi_2}| \tag{12}$$

The system equations are nonlinear, as the stiffness and loss factor of the WRI depend on the vibration response. Iterative solution method is used to solve the system response, where the effective stiffness k_{eff} and loss factor η of the WRI depend on the amplitude x_a from previous iteration. The simplest iteration scheme is as follows:

1. Define initial value for the vibration amplitude x_a.
2. Calculate the values of k_{eff} and η based on x_a (Eqs. (4) and (6)).
3. Solve the system response (Eq. (10)).
4. Calculate the vibration amplitude (Eq. (12)).
5. Check convergence by calculating the difference between the amplitude x_a from previous and current iteration.
6. If the convergence criterion is met, the solution is finished. Otherwise return to step 2 starting from the calculated x_a value.

The convergence criterion should be set significantly smaller than the estimated response. However, if the convergence criterion is too small, the scheme might not converge. More sophisticated methods such as gradient based methods can be used to avoid convergence issues. This method is valid for only steady state response, as all of the nonlinear parameters have been defined as a function of vibration amplitude.

The model implementation was validated using an example single degree of freedom model. The arbitrarily selected validation model parameters are presented in Tables 1–3. The resulting amplitude was obtained by iteratively solving Eq. (8) until the displacement converged. The process was repeated for a range of forces up to maximum F_{max} given in Table 1. The whole process was repeated with three different loading frequencies, to show that the stiffness and damping are in fact frequency independent. The final converged stiffness and loss energy values were plotted against the hand calculated reference values.

Table 4
Main dimensions of the wire rope isolator investigated in this study.

Dimension	Value
Loop width	58 mm
Loop height	32 mm
Number of wire rope loops	2
Strand lay length	34 mm
Wire rope diameter	5 mm
Wire type	7 × 19
Wire material	AISI 316L
Strand diameter	1.65 mm

Table 5
Information on the used measurement equipment.

Sensor	Model	Sensitivity	Linearity error
Accelerometers	PCB602D01	10.2 mV/(m/s^2)	±1%
Force transducer 1	WIKA F2808-1000N	(2.0 ± 0.2) m V/V	±0.15 %F$_{nom}$
Force transducer 2	WIKA F2812-1000N	(2.0 ± 0.2) m V/V	±0.5 %F$_{nom}$

Table 6
Components used in the test setups.

Component	Information
Preload mass	Steel plates, m = maximum 8 kg per WRI
Excitation mass	Steel plate, m = 5 kg
Frame	BSB Aluminium profile 50 × 50
Stinger	M5 steel rod
Exciter	Electro-magnetic shaker Siocera JZK-100
Signal generator	OWON AG 1011F
Decoupling springs	Helical steel spring (k = 8500 N/m)

3. Experiments

To fit the parameters of the mathematical model, to verify its performance, and to study the effect of preload and loading frequency, experimental measurements were conducted. The study was performed with a single WRI design. Two different measurement setups were used, one for parameter fitting, and one for model verification. This chapter presents the investigated WRI, followed by measurement design. Finally the measurement analysis process including the parameter fitting process is presented.

3.1. Investigated wire rope isolator

A single WRI design was selected for the experimental part of the study. The main dimensions of the investigated WRI unit are given in Table 4 and their meaning is presented in Fig. 1. The WRI selected for this study is a small one, with two wire rope loops between the bars. There are numerous possible configurations, as the number and size of the loops as well as the size and type of WRI can be almost freely selected. For this study, a smaller size WRI was selected as it requires smaller measurement setup. The selected WRI does not necessarily provide optimal balance between stiffness and damping.

The WRIs used in this study were first worn in, as the stiffness and damping of the WRI change as the wires and strands wear from the internal friction. The roughness difference resulting from the wear between unused and worn wire ropes can be felt by hand. The WRIs were worn in to better match the real operational state of the WRI. Initially the decrease is faster, but after some time the reduction saturates.

3.2. Measurement design

To study the dynamics of the WRI, the vibration response of the WRI was studied under two different measurement setups. These are the forced response measurement (direct measurement), and a base excitation measurement (indirect measurement). The measurement schematics are presented in Figs. 5 and 7. In these measurements, the WRIs

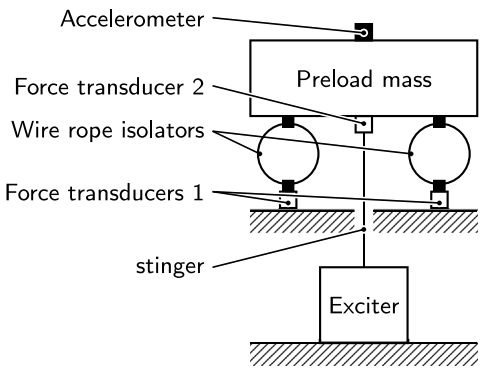

Fig. 5. Illustration of the direct test setup, which was used to determine the parameters for the proposed model. The setup has in total four WRIs. The force transducers were used to measure the forces transmitted through each of the wire rope isolators. Accelerometer was used to measure the movement of the preload mass. Electromagnetic shaker was used to excite the preload mass.

were mounted to a frame with applied preload. The amount of preload was varied between the measurements. The excitation was applied with an electromagnetic shaker. The shaker was used to create amplitude sweeps with constant frequency and frequency sweeps with constant amplitude. The forces were measured using force transducers, and the displacements were measured using accelerometers, listed in Table 5.

In both measurement setups, the tested WRIs were mounted onto a frame made from aluminium profiles and steel plates, and a preload mass in a form of steel plates was attached on the top to apply the preload. Four WRIs were used simultaneously in a symmetric configuration, to minimize the horizontal and rotational motion of the preload mass. The excitation was applied on the center of the preload mass using an electromagnetic shaker through a stinger. This was necessary to prevent the transfer of horizontal loads to the shaker. A displacement based control was used, and there was no feedback from the measurement rig to the shaker. The components used in the test setup are listed in Table 6.

In the direct test setup the excitation force was applied directly on the preload mass on top of the WRI, and in the indirect test setup the excitation force was applied in the form of base excitation. During the measurements, the excitation amplitude and frequency were varied, along with the WRI preload. The forces and accelerations were measured at a sampling rate of 10 kHz. Force transducers were placed under each WRI and also to the stinger which loaded the WRI. Accelerometers were placed on the preload mass as well as on the base of the test setup. Multiple simultaneous acceleration measurement locations were used to avoid errors arising from the local movement of the masses.

The test setup of the direct measurement is presented in Fig. 6 and the schematic on Fig. 5. The test setup follows the test setup defined in ISO 10846-2 [31], but is not completely according to the standard. While the measurement was made with four WRIs in symmetric condition, which allows to create the mathematical model for only one WRI as a 1-DOF model shown in Fig. 3. A preload mass was installed on top of the WRIs prior to loading, and no guides were installed on the mass. During the direct measurements, the loading frequency was kept constant, and the loading amplitude was decreased from maximum to zero during a 60 s time period. The test was repeated with multiple excitation frequencies. The maximum amplitude had to be limited with maximum preload and frequency values due to the resonance frequency of the WRI.

The measurement setup for the indirect measurement is presented in Fig. 8 and the schematic on Fig. 7. This setup differs from the direct measurements by placing the WRIs on top excitation mass instead of the frame, and the loading was applied on the excitation mass instead of the preload mass. The test setup follows the setup defined in ISO 10846-3 [32], but is not completely according to the standard. The

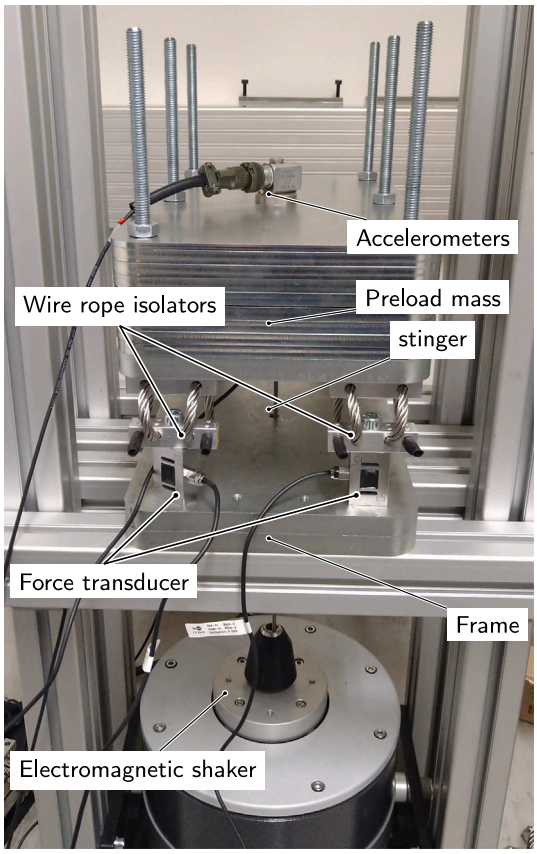

Fig. 6. Test setup used in direct test, which was used to determine the parameters for the proposed model. The test setup corresponds to a forced excitation case. The test setup consists of a frame, four WRIs, preload mass and the electromagnetic shaker. The electromagnetic shaker was connected to the preload mass, which was placed on top of four WRIs. The WRIs were attached to the supporting frame, with force sensors in between. Accelerometer was used to measure the movement of the preload mass.

preload mass was supported only by the WRIs, and was free to move in all directions. The excitation mass is placed on top of 18 helical springs that act as dynamical decoupling springs. The excitation mass was a steel plate weighing 7.5 kg. During the measurement, the loading frequency was swept from 15 Hz to 100 Hz during a 200 s period, while the electromagnetic exciter force was kept constant through constant input voltage. Open-loop control was used. The test is repeated with different force amplitudes to measure the effect of vibration amplitude to the behavior of WRI.

3.3. Measurement analysis

The mathematical model has several parameters that have to be tuned based on experiments. These are the coefficients for the polynomials of amplitude dependent stiffness and loss energy. The tuning is performed using the results from the direct measurements. The stiffness can be calculated directly from the force and displacement signals, by calculating the effective amplitudes of each quantity as defined in Section 2. The loss energy for each amplitude is calculated from the area of the measured hysteresis loop. To fit the loss energy and stiffness models, the measured quantities are the plotted as a function amplitude, and the curves are fitted to the data as defined in Section 2.

The parameter fitting process was performed using the whole dataset for a said preload level, as well as using a single loading frequency. A gradient based optimization method was used to fit the parameters. The least squares residual was calculated for each function at all measured amplitudes. The residual is the sum of differences

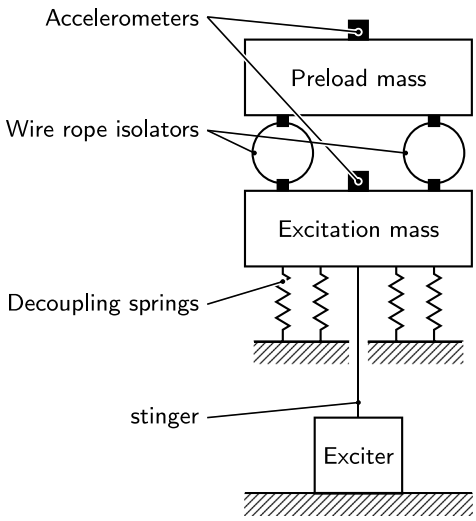

Fig. 7. Illustration of the indirect test setup, which was used to verify the performance of the proposed model. The accelerations of the preload mass and excitation masses were measured, to calculate the amplification factor under varying loading frequency. The mass of excitation mass is 8 kg. In total 18 decoupling springs were used.

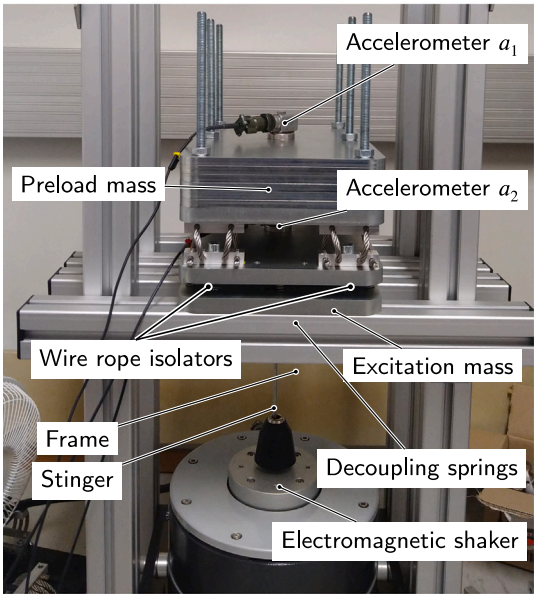

Fig. 8. Test setup used in the indirect test, which was used to verify the performance of the proposed model. The test setup corresponds to a base excitation case. The test setup consists of a frame, decoupling springs, excitation mass, four WRIs, preload mass and the electromagnetic shaker. The electromagnetic shaker was connected to the excitation mass, which was placed on top of the supporting frame using decoupling springs. The WRIs and the preload were placed on top of the excitation mass. Accelerometers were placed on the excitation mass and preload mass to measure the movement of the masses. The preload mass was free to move along the loading axis.

between the measured values at certain amplitude and the values given by the equation at the same amplitude. The residual was minimized by optimizing the parameter values of each function (Eqs. (4), (3)). For the loss energy function (Eq. (3)), the fitting was performed separately for each part of the function. The optimization process was repeated with varying values of the threshold amplitude $x_{\text{threshold}}$, and the value with smallest total residual was selected. The effect of preload and frequency on the fitted coefficients was compared by plotting the coefficients as a function of preload and frequency.

To verify that the mathematical model works as intended, it was compared to measurements from the indirect measurement. The indirect measurement is not used to define the parameters of the mathematical model. From the measurement, the vibration amplitudes of the excitation mass and preload mass were measured during the frequency sweep, and amplification factor was calculated. The measured amplification factor was compared to the simulated amplification factor. The simulated amplification factor was calculated using the equations presented in Section 2.

4. Results

The results from the measurements and mathematical model are presented in this section. Mathematical model validation was done to ensure correct behavior of model implementation. The mathematical model was fitted using the data from the direct test, and indirect test results were used to verify the performance of the mathematical model.

4.1. Validation

The mathematical model is validated using a 1-DOF example model with parameters given in Tables 1–3. Here, the response is calculated with increasing force using the iterative method, and the resulting stiffness and loss energy values are compared on to the predetermined curve to show that the model implementation behaves as desired. The resulting effective stiffness, loss energy are shown as the function of WRI amplitude in Fig. 9. With three different loading frequencies, the response of the model is similar. The loss energy and stiffness curves show desired behavior, the response is rate independent and the increasing amplitude results in desired shapes of the stiffness and loss energy curves. These indicate that the implemented model works as intended. The model verification with experimental data is shown in following sections.

4.2. Parameter fitting

This section presents the results from the parameter fitting from the direct measurement. The loading amplitude and frequency, as well as preload were varied during the measurements. The effective stiffness and loss energy values were determined from the measured hysteresis loops. The energy was obtained from the area swept by the curve, while the stiffness was obtained from the end points of the hysteresis loop. Example hysteresis curve is shown in Fig. 10 with three load levels at 8 kg preload and 25 Hz loading frequency. Fig. 11 shows the hysteresis loops with varying preload and frequency. The phase space response for two cases with different load frequencies are shown in Fig. 12. The effect of preload was small, and is therefore not shown in Fig. 12. The loss energy of WRIs was obtained from the direct test, and the results are shown in Fig. 13 with different preload levels. The loss energy was calculated from the area of the hysteresis loop, of which an example is shown in Fig. 10. From Fig. 13 we see that the preload and excitation frequency have some effect on the loss energy of the WRI, but the effect is less significant than the effect of vibration amplitude. The effect of frequency and preload increase as the amplitude grows. A curve is fitted onto the measured data as stated in Section 2, and the resulting fit is shown in Fig. 14. The Fig. 14 shows that the proposed model fits well with the measurements.

The effective stiffness was calculated from the maximum and minimum forces and displacements of the hysteresis curves. The measured effective stiffness values from the measurements are presented in Fig. 15. Third order polynomial function was fitted onto the data. The stiffness results are presented in Fig. 16, along with the effective stiffness on the compression and tension sides of the hysteresis curves. The Figure shows that the stiffness decreases as the vibration amplitude increases, and that the rate of softening decreases as the amplitude grows. The excitation frequency affects the measured effective stiffness

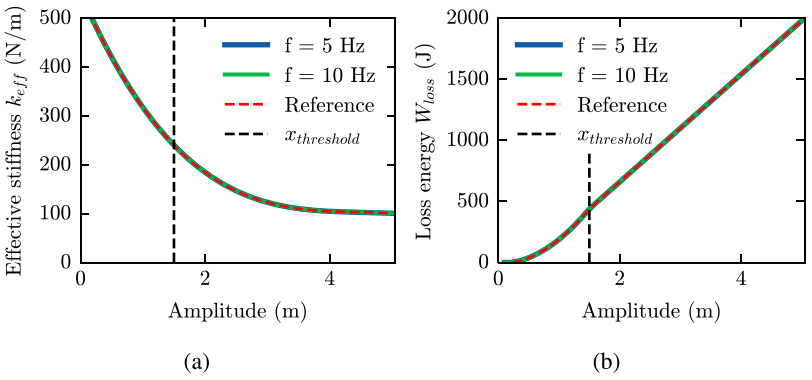

Fig. 9. The effective stiffness (a) and loss energy (b) from model validation using a 1-DOF model. The stiffness curve follows the defined third order polynomial, and the loss energy follows the piece-wise defined function. Vertical dashed line shows the amplitude at which the loss energy function changes the piece-wise defined.

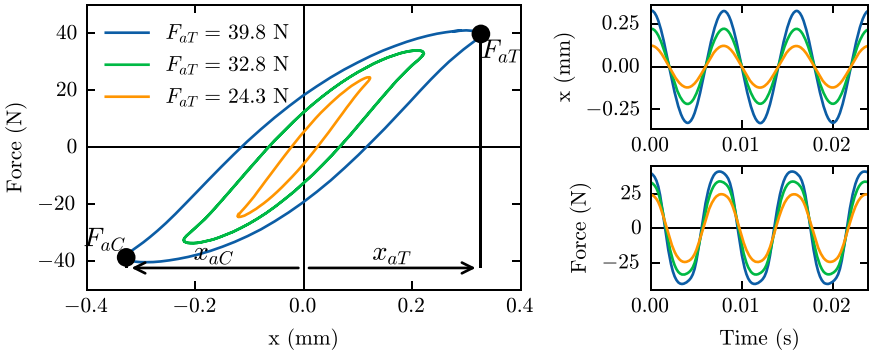

Fig. 10. Hysteresis curves from the direct test, with 8 kg preload and 25 Hz excitation frequency. The increased hysteresis can be seen clearly with increasing loading. The small panel figures show the time history data from the hysteresis loops.

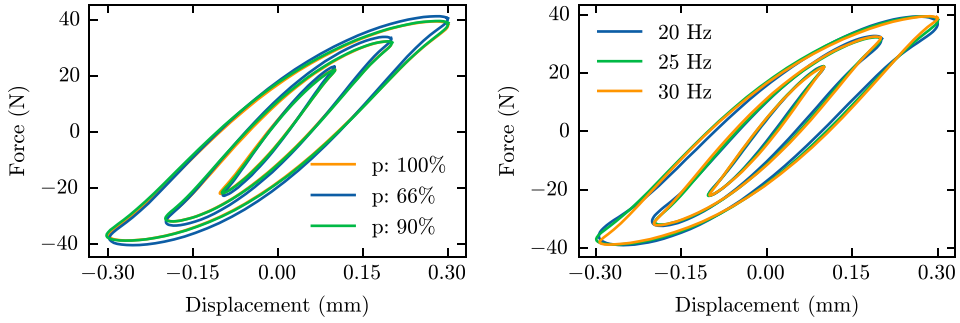

Fig. 11. Hysteresis curves from the direct test. Figure on the left shows curves with varying preload (p) at 25 Hz loading frequency, while the figure on the right shows the curves with varying loading frequency at 8 kg preload. The amplitudes of the curves are 0.1, 0.2 and 0.3 mm.

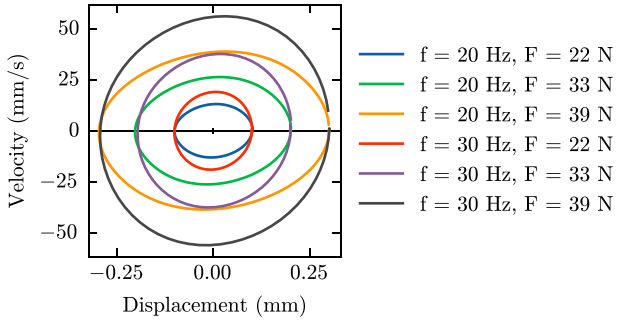

Fig. 12. The phase space diagram from the measurements at three displacement amplitudes with loading frequencies of 20 Hz and 30 Hz are shown.

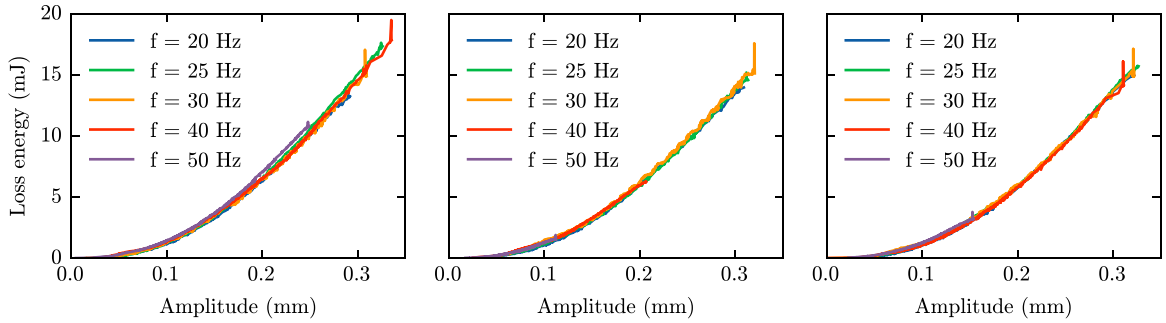

Fig. 13. Loss energy calculated from the measured hysteresis loops with different preload levels (5.3, 7.2 and 8 kg) as a function of vibration amplitude.

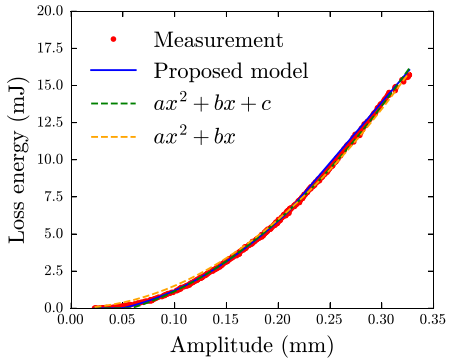

Fig. 14. Measured loss energy as a function of amplitude, with the proposed model fit and a purely second order fit. The measurement data is with 25 Hz loading frequency at 8 kg preload.

of the WRI, and its effect increases with higher excitation amplitudes. This contradicts with the assumption that the WRI is totally rate independent, but the effect is small when compared to the effect of excitation amplitude. With smaller excitation amplitudes the rate independent behavior is a reasonable assumption.

The loss factor for the system was calculated from the measured loss energy and the effective stiffness as a function of vibration amplitude, as shown in Fig. 17. The loss factor was also calculated using the mathematical model with matching vibration amplitudes. Both results are shown in Fig. 18. With very small amplitudes the loss factor is 0, as the WRI behaves elastically. The mathematical model fits better at higher amplitudes. The error in the loss factor at lower amplitudes comes from the large relative error in the loss energy between the measured and calculated ones. The loss factor has an opposite trend when compared to observations by [25,26]. With larger amplitudes the loss factor would most likely start to decrease due to the increasing stiffness.

The effect of loading frequency and preload on the loss energy was studied by measuring the loss energy with different preload values and loading frequencies, and fitting the energy loss W_{loss} to each of the measurements. The resulting coefficients are plotted as a function of loading frequency in Fig. 19(a) and (b) for second order polynomial. Fig. 19(f) shows the transition displacement, at which the energy loss model changes from second order polynomial to first order polynomial and Fig. 19(c) the constant coefficient for the second order polynomial. Fig. 19(d) and (e) shows the effect on the coefficients for first order polynomial. The figures show that there is notable variation in the coefficient values, but no clear trend.

4.3. Verification

The indirect test measured the amplification of the WRI under base excitation with different load amplitudes. Fig. 20 shows the measured amplifications as a function of excitation frequency along with the simulated ones, and the key results are summarized in Table 7. The figure shows that maximum amplification at resonance decreases as the base excitation level increases. The increased base excitation leads to higher vibration amplitude which in turn leads to the increasing damping in the WRI. The increasing amplitude also causes the effective stiffness to decrease, which decreases the resonance frequency. Higher loss energy widens the resonance peak.

5. Discussion

The proposed mathematical model agreed well with the measured loss energy and stiffness data. The model parameters were determined using industry standard tests, meaning that creating new WRI designs and corresponding calculation models is easy and efficient. No additional tuning parameters were necessary to better align the results. The values obtained with least squares fit were used throughout the study.

When looking at the loss energy W_{loss} curve in Fig. 14, we see that the new model fits similarly well as does the second order polynomial with the constant term. The fit without the constant term is almost as good, but slightly worse at smaller amplitudes. However, when calculating the loss factor in Fig. 18, the difference becomes clear. The loss factor without the constant term gives notably less accurate results at small amplitudes. The proposed model gives the best match to the measurement data. The loss energy measured shows similar amplitude dependent trend that [33] observed for loss energy due to cable bending. Under small amplitudes, the wire ropes bend more rather than elongate, leading to similar results.

Interestingly that the loss factor seems to stabilize at some value at certain displacement. It is most likely, that eventually the loss factor starts to decrease again due to the increasing effective stiffness. This decrease would match the observations in the research of [34]. Based on the loss factor curve there is a certain amplitude range and therefore a loading range, at which the WRI has the best damping properties. This would provide interesting topic for future research.

From Fig. 13, we see that the overall effect of loading frequency on the loss energy is small, while the preload has more significant impact. Similar observation can be made from the hysteresis curves shown in Fig. 11. The effect was further studied by fitting the model to each test, and comparing the values. From Fig. 19(a) and (b) we see that there is not a clear trend on how the frequency affects each coefficient. There is a somewhat parabolic trend with b_2, c_2, $x_{\text{threshold}}$ and c_1, while the coefficients a_1 and b_1 do not have anything resembling a function. The effect of preload is less clear on the parameters, especially between 7.2 kg and 8 kg preload levels. At some amplitudes the 7.2 kg preload yields higher coefficient values, but at some 8 kg yields higher values. In Fig. 19(a) we see that the 8 kg preload has larger coefficient a_1 with excitation frequencies 20, 25 and 50 Hz, but smaller with 30 and 40 Hz. The difference between actual preload value in this case is very small, 7.2 kg and 8 kg, which might explain the differences.

When looking at Figs. 15 and 13, it is clear that increasing preload causes small decrease in the loss energy and the effective stiffness.

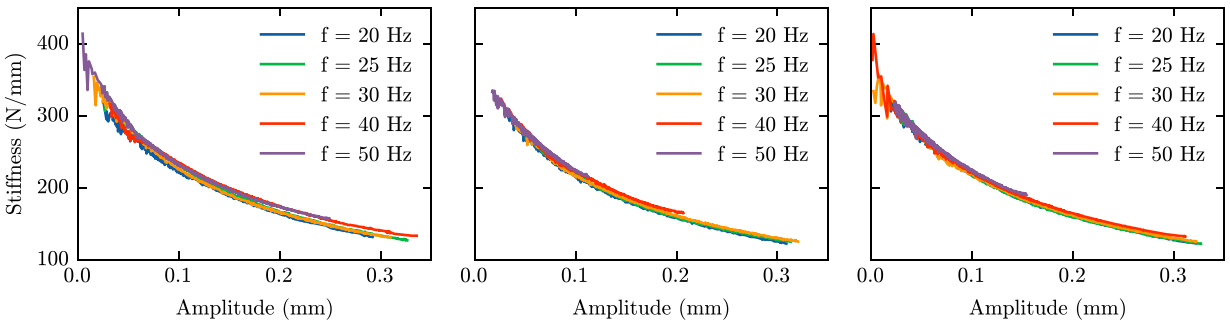

Fig. 15. Effective stiffness from the measurements with different preload levels (5.3, 7.2 and 8 kg) as a function of amplitude.

Table 7
The loads and results from the indirect test used for verification of the mathematical model.

Case number	Base velocity at resonance [mm/s]	Measured frequency of max amplification [Hz]	Calculated frequency of max amplification [Hz]	Measured max amplification [–]	Calculated max amplification [–]
1	2.28	27	29	4.1	4.4
2	6.77	24	24	2.8	2.9
3	11.35	23	23	2.0	2.1
4	14.30	22	23	1.9	2

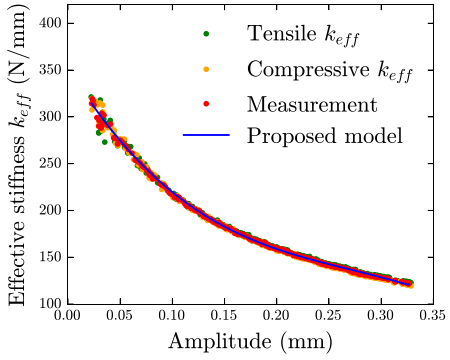

Fig. 16. Measured effective stiffness as a function of amplitude, with the proposed third order fit. The measurement data is with 25 Hz loading frequency at 8 kg preload. The tensile and compressive k_{eff} present the effective stiffness calculated from the tensile and compressive sides of the hysteresis curve. It becomes clear that at these vibration amplitudes the hysteresis curve is almost symmetric as they yield similar values.

This does not show in the fitting parameters as seen in Fig. 19, most likely due to non optimal fit of the parameters and due to fact that the difference is very small. This is also shown in Fig. 11. The effect of loading frequency is very small with all levels of preload.

The mathematical model was verified against the results from indirect measurements, and shown to give good results (Fig. 20). The calculated results have roughly correct resonance frequencies and amplitudes when compared to the measurements. The WRI shows softening behavior, where the resonance frequency decreases as the vibration amplitude increases. Similar behavior has been observed in [35]. In addition to the resonance frequency decreasing, the amplification factor decreases with increasing loading amplitude.

As was shown, the loss factor has a vibration amplitude range where the damping properties are best. Since these depend on the load magnitude, the required amount of dimensioning curves would be huge. The relatively simple measurement setup allows to test a large number of different WRI configurations, which could be used to better study for example the effect of wire rope diameter on the dynamics. The proposed model could be implemented to commercial finite-element programs, by using the presented iterative solution method.

The proposed model has multiple limitations. The model provides results only under small displacements, and is not applicable for transient cases. For loading cases falling under these conditions, more accurate models are needed. Additionally, the model parameters are defined using experimental measurements, meaning that the measurements have to be repeated for each WRI design, which can be tedious with multiple designs. For practical simulation problems using commercial FE-programs, the iterative solution can be performed by adjusting the WRI values by hand. This is tedious, but could also be implemented with some scripting work. No new elements are necessary, as a linear spring element will suffice with the iterative solution method. The loss factor η can be converted into viscous damping coefficient using text book equations [30].

The fit of the mathematical model was the poorest with very small amplitudes. When the amplitudes are very small, even small errors can become significant. Additionally, the influence of measurement setup becomes more significant. There could be some small flexibility in the measurement setup. The model agrees relatively well even at these ranges. Other source for error between calculation and measurement can be traced to the curve fitting, where the proposed model does not perfectly align with the measurement. Alternative fitting algorithms could solve this problem.

In the future, the tests should be repeated with more tightly spaced loading frequencies and preload values. Additionally, the maximum loading amplitude should be increased to determine if the loss factor indeed starts to decrease. With the present WRI design, the natural frequency of the WRI limits the amplitudes at higher frequencies. In addition, to study the statistical nature of the problem, multiple units of the WRI should be used.

6. Conclusions

A new model is proposed for steady-state axial response calculation of wire rope isolators (WRI). The nonlinear dynamics of the WRI can be linearized with respect to small-variations in vibration amplitude. The model is shown effective under the assumption of small-amplitude vibrations, which represents the primary use case. The effects of excitation frequency and preload on the steady-state response are found to be minor in comparison those of the amplitude. The proposed model is highly effective in reproducing the WRI response characteristics, and its parameters can be defined with an industry standard testing setup.

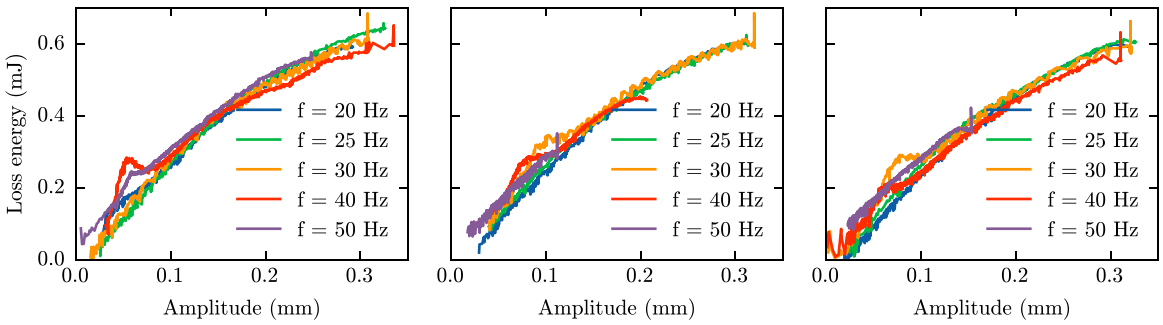

Fig. 17. Loss factor as a function of amplitude calculated from measured stiffness and loss energy from the measurements with different preload levels (5.3, 7.2 and 8 kg).

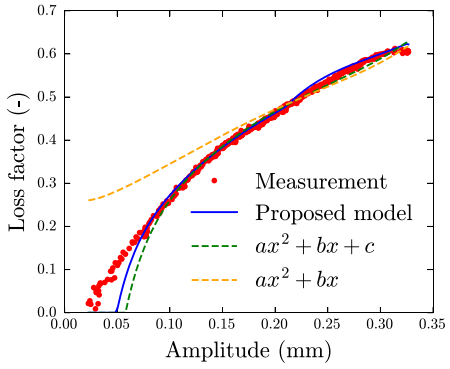

Fig. 18. The loss factor as a function of amplitude calculated from measured stiffness and loss energy using Eq. (6). The measurement data is with 25 Hz loading frequency at 8 kg preload. The fit is calculated using the proposed model fit and a purely second order fit with and without the constant coefficient as the functions for loss energy. The second order polynomial without c corresponds to model proposed by [26].

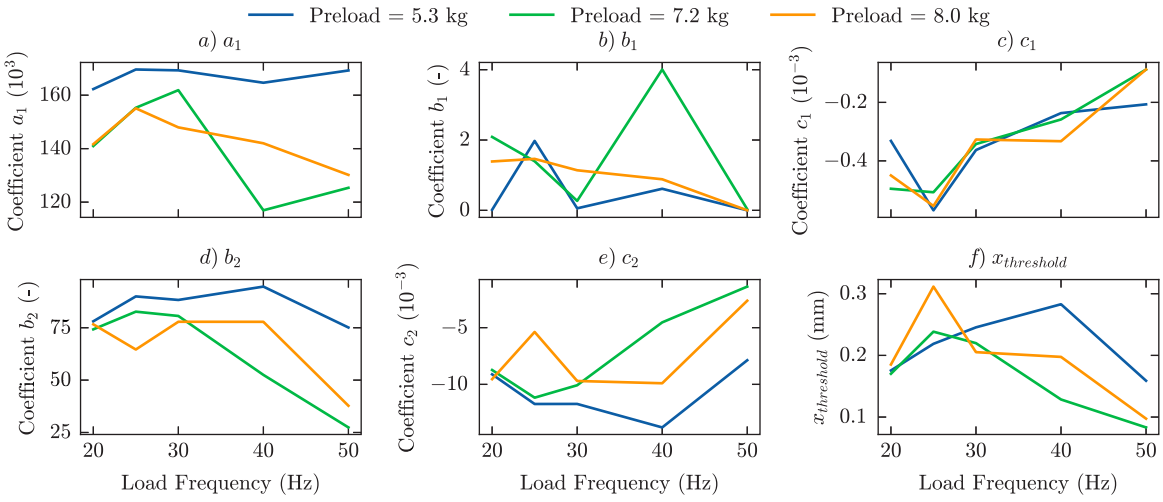

Fig. 19. The effect of preload level and loading frequency on the coefficients of the proposed W_{loss} model. The coefficients are given in Eq. (3).

CRediT authorship contribution statement

Samuli Rytömaa: Writing – review & editing, Writing – original draft, Visualization, Validation, Software, Methodology, Investigation, Formal analysis, Conceptualization. **Olli Malmi:** Writing – review & editing, Methodology, Investigation, Data curation, Conceptualization. **Sampo Laine:** Writing – review & editing, Writing – original draft, Software, Methodology, Investigation. **Jarkko Keinänen:** Project administration, Methodology, Conceptualization. **Raine Viitala:** Writing – review & editing, Supervision, Project administration, Funding acquisition.

Declaration of competing interest

The authors declare that they have no known competing financial interests or personal relationships that could have appeared to influence the work reported in this paper.

Data availability

The data that has been used is confidential.

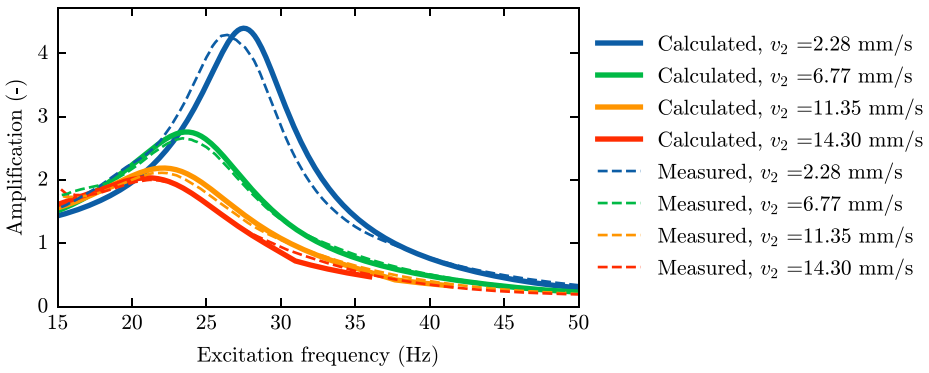

Fig. 20. Amplification factors from the measured and simulated indirect tests as a function of excitation frequency. The amplification decreases with increasing loading amplitude due to increase in the loss factor showing softening behavior. The measured results are presented with the dashed lines, while the simulated ones are with solid lines. The difference between each color is the loading magnitude, and the results are also summarized in Table 7. The velocity of the excitation mass at maximum amplification is given in the legend.

References

[1] Ibrahim R. Recent advances in nonlinear passive vibration isolators. J Sound Vib 2008;314:371–452. http://dx.doi.org/10.1016/j.jsv.2008.01.014.

[2] Milovanovic Z, Kovacic I, Brennan MJ. On the displacement transmissibility of a base excited viscously damped nonlinear vibration isolator. J Vib Acoust 2009;131(5):054502. http://dx.doi.org/10.1115/1.3147140.

[3] Laalej H, Lang ZQ, Daley S, Zazas I, Billings SA, Tomlinson GR. Application of non-linear damping to vibration isolation: an experimental study. Nonlinear Dynam 2012;69(1–2):409–21. http://dx.doi.org/10.1007/s11071-011-0274-1.

[4] Sun J, Huang X, Liu X, Xiao F, Hua H. Study on the force transmissibility of vibration isolators with geometric nonlinear damping. Nonlinear Dynam 2013;74:1103–12. http://dx.doi.org/10.1007/s11071-013-1027-0.

[5] Zhang Z, Zhang Y-W, Ding H. Vibration control combining nonlinear isolation and nonlinear absorption. Nonlinear Dynam 2020;100:2121–39. http://dx.doi.org/10.1007/s11071-020-05606-6.

[6] Tinker ML, Cutchins MA. Damping phenomena in a wire rope vibration isolation system. J Sound Vib 1992;157:7–18. http://dx.doi.org/10.1016/0022-460X(92)90564-E.

[7] Vinogradov OG, Atatekin IS. Internal friction due to wire twist in bent cable. J Eng Mech 1986;112(9):859–73. http://dx.doi.org/10.1061/(ASCE)0733-9399(1986)112:9(859).

[8] Lanteigne J. Theoretical estimation of the response of helically armored cables to tension, torsion, and bending. J Appl Mech 1985;52(2):423–32. http://dx.doi.org/10.1115/1.3169064.

[9] Papailiou KO. Bending of helically twisted cables under variable bending stiffness due to internal friction, tensile force and cable curvature. October 1995;168.

[10] Jolicoeur C. Comparative study of two semicontinuous models for wire strand analysis. J Eng Mech 1997;123:792–9. http://dx.doi.org/10.1061/(ASCE)0733-9399(1997)123:8(792).

[11] Ledezma-Ramírez DF, Tapia-González PE, Ferguson N, Brennan M, Tang B. Recent advances in shock vibration isolation: An overview and future possibilities. Appl Mech Rev 2019;71(6):060802. http://dx.doi.org/10.1115/1.4044190.

[12] Demetriades G, Constantinou M, Reinhorn A. Study of wire rope systems for seismic protection of equipment in buildings. Eng Struct 1993;15(5):321–34. http://dx.doi.org/10.1016/0141-0296(93)90036-4.

[13] Ni YQ, Ko JM, Wong CW, Zhan S. Modelling and identification of a wire-cable vibration isolator via a cyclic loading test. Proc Inst Mech Eng I 1999;213:163–72. http://dx.doi.org/10.1243/0959651991540052.

[14] Alessandri S, Giannini R, Paolacci F, Amoretti M, Freddo A. Seismic retrofitting of an HV circuit breaker using base isolation with wire ropes. Part 2: Shaking-table test validation. Eng Struct 2015;98:263–74. http://dx.doi.org/10.1016/j.engstruct.2015.03.031.

[15] Bouc R. Modèle mathématique d'hystérésis. Acustica 1971;21:16–25.

[16] Wen Y-K. Method for random vibration of hysteretic systems. J Eng Mech Div 1976;102(2):249–63. http://dx.doi.org/10.1061/JMCEA3.0002106.

[17] Salvatore A, Carboni B, Chen LQ, Lacarbonara W. Nonlinear dynamic response of a wire rope isolator: Experiment, identification and validation. Eng Struct 2021;238:112121. http://dx.doi.org/10.1016/J.ENGSTRUCT.2021.112121.

[18] Vaiana N, Sessa S, Rosati L. A generalized class of uniaxial rate-independent models for simulating asymmetric mechanical hysteresis phenomena. Mech Syst Signal Process 2021;146:106984. http://dx.doi.org/10.1016/j.ymssp.2020.106984.

[19] Barbieri N, Barbieri R, da Silva RA, Mannala MJ, Barbieri LdV. Nonlinear dynamic analysis of wire-rope isolator and Stockbridge damper. Nonlinear Dynam 2016;86(1):501–12. http://dx.doi.org/10.1007/S11071-016-2903-1/FIGURES/16, Publisher: Springer Netherlands.

[20] Paolacci F, Giannini R, De Angelis M. Seismic response mitigation of chemical plant components by passive control techniques. J Loss Prev Process Ind 2013;26(5):924–35. http://dx.doi.org/10.1016/j.jlp.2013.03.003.

[21] Balaji PS, Moussa L, Rahman ME, Vuia LT. Experimental investigation on the hysteresis behavior of the wire rope isolators. J Mech Sci Technol 2015;29:1527–36. http://dx.doi.org/10.1007/S12206-015-0325-5/METRICS.

[22] Alessandri S, Giannini R, Paolacci F, Malena M. Seismic retrofitting of an HV circuit breaker using base isolation with wire ropes. Part 1: Preliminary tests and analyses. Eng Struct 2015;98:251–62. http://dx.doi.org/10.1016/j.engstruct.2015.03.032.

[23] Spizzuoco M, Quaglini V, Calabrese A, Serino G, Zambrano C. Study of wire rope devices for improving the re-centering capability of base isolated buildings. Struct Control Health Monit 2017;24(6):e1928. http://dx.doi.org/10.1002/stc.1928.

[24] Xie Q, Yang Z, He C, Xue S. Seismic performance improvement of a slender composite ultra-high voltage bypass switch using assembled base isolation. Eng Struct 2019;194:320–33. http://dx.doi.org/10.1016/j.engstruct.2019.05.055.

[25] Pellecchia D, Vaiana N, Spizzuoco M, Serino G, Rosati L. Axial hysteretic behaviour of wire rope isolators: Experiments and modelling. Mater Des 2023;225:111436. http://dx.doi.org/10.1016/j.matdes.2022.111436.

[26] Gerges RR, Vickery BJ. Design of tuned mass dampers incorporating wire rope springs: Part I: Dynamic representation of wire rope springs. Eng Struct 2005;27:653–61. http://dx.doi.org/10.1016/J.ENGSTRUCT.2004.12.015.

[27] Lai K, Fan W, Chen Z, Yang C, Liu Z, Li S. Performance of wire rope damper in vibration reduction of stay cable. Eng Struct 2023;278:115527. http://dx.doi.org/10.1016/J.ENGSTRUCT.2022.115527, Publisher: Elsevier.

[28] Balaji PS, Rahman ME, Moussa L, Lau HH. Wire rope isolators for vibration isolation of equipment and structures – A review. IOP Conf Ser: Mater Sci Eng 2015;78:012001. http://dx.doi.org/10.1088/1757-899X/78/1/012001.

[29] Spak K, Agnes G, Inman D. Cable modeling and internal damping developments. Appl Mech Rev 2013;65. http://dx.doi.org/10.1115/1.4023489/694606.

[30] Inman DJ. Engineering vibration. Upper Saddle River: Pearson; 2014.

[31] International Organization for Standardization. Acoustics and vibration — Laboratory measurement of vibro-acoustic transfer properties of resilient elements —Part 2: Dynamic stiffness of elastic supports for translatory motion — Direct method. Standard, 1997.

[32] International Organization for Standardization. Acoustics and vibration - Laboratory measurement of vibro-acoustic transfer properties of resilient elements - Part 3: Indirect method for determination of the dynamic stiffness of resilient supports for translatory motion. Standard, 2002.

[33] Foti F, Martinelli L. A unified analytical model for the self-damping of stranded cables under aeolian vibrations. J Wind Eng Ind Aerodyn 2018;176:225–38. http://dx.doi.org/10.1016/j.jweia.2018.03.028.

[34] Guzmán-Nieto M, Tapia-González PE, Ledezma-Ramírez DF. Low frequency experimental analysis of dry friction damping in cable isolators. J Freq Noise Vibr Active Control 2015;34(4):513–24. http://dx.doi.org/10.1260/0263-0923.34.4.513.

[35] Gürses K, Acar B, Özgen GO. Experimental investigation of amplitude dependent behaviour of a wire rope isolator system using modal testing methods. In: International conference on noise and vibration engineering - ISMA2022. 2022, p. 2454–68.